Energy Storage Materials xxx (xxxx) xxx

Contents lists available at ScienceDirect

Energy Storage Materials

journal homepage: www.elsevier.com/locate/ensm

A low-cost intermediate temperature Fe/Graphite battery for grid-scale energy storage

Tao Dai [a], Lie Yang [a], Xiaohui Ning [a,*], Danli Zhang [a], R. Lakshmi Narayan [b], Ju Li [c,**], Zhiwei Shan [a]

[a] Center for Advancing Materials Performance from the Nanoscale (CAMP-Nano), State Key Laboratory for Mechanical Behavior of Materials, Xi'an Jiaotong University, Xi'an, 710049, PR China

[b] Department of Materials Science and Engineering, Indian Institute of Technology, Delhi, 110016, India

[c] Department of Nuclear Science and Engineering, Department of Materials Science and Engineering, Massachusetts Institute of Technology, Cambridge, MA, 02139, USA

ARTICLE INFO

Keywords:
Fe/graphite battery
Intermediate temperature
Low-cost
Dendrite-free
Molten salt

ABSTRACT

Due to their compactness, storage/supply flexibility, modularity and factory manufacturability, batteries are excellent candidates for large scale energy storage applications. However, the widespread application of most batteries hitherto developed is hindered by their high cost. Here, an intermediate temperature molten salt battery is developed that emphatically resolves this issue by using all earth-abundant and cheap elements. Operated at 170 °C, the cell comprises of an Fe metal anode, NaCl saturated $NaAlCl_4$ electrolyte and an $AlCl_4^-$ intercalated graphite cathode in the fully charged state. It has a capacity retention of 85% after nearly 10,000 cycles. After characterizing the anode, it was determined that the high reversibility of the Fe to $FeCl_2$ solid state transformation are responsible for the absence of dendritic growth on such a metal anode. Different electrode capacity matching strategies are discussed in the context of ensuring safe operation during overcharging. Finally, the overall material cost of the Fe/Graphite cell is estimated to be 33.9 $ kWh^{-1}, which can potentially meet the demands of the commercial energy storage market.

1. Introduction

Amongst different large-scale stationary electrical energy storage devices, batteries provide very high spatial and temporal flexibility in managing electrical energy. This is because, in addition to being compact and modular (truckable from factory, instead of civil construction), which facilitates easy physical storage at a variety of locations, they also have the ability to store and supply electrical energy with almost zero latency. Therefore, an electrical power grid that integrates them with renewable energy sources will be highly reliable and efficient [1–3]. Despite these advantages, most of the existing batteries are expensive and their extensive use in large-scale power grids is still uncommon [4,5].

Recently, molten salt batteries, like Na–S batteries, sodium metal halide (ZEBRA, Zeolite Battery Research Africa) batteries and liquid metal batteries, all of which operate at elevated temperatures (300°C–500 °C), have been incorporated in grid scale energy storage applications, mainly due to their enhanced rate performances [6–11]. However, operating these devices at elevated temperatures poses a unique set of challenges. One of these challenges pertains to identifying suitable but inexpensive materials for sealing the structure electrically and thermally [10,12,13]. Limiting heat dissipation related losses is particularly important because doing so not only saves cost but also enhances the battery's long-term energy efficiency [14,15]. To address these challenges, some studies have lowered the operating temperature of batteries to the 'intermediate' temperature range (below 250 °C), such as the intermediate-temperature (~150 °C) Na–S battery reported by Lu et al., the intermediate-temperature (190 °C) sodium–nickel chloride batteries demonstrated by Li et al., and the intermediate-temperature (240 °C) liquid metal battery proposed by Jin et al. [12,16,17]. In this way, the corrosion and sealing issues are much easier to deal with, leading to lower capital expenditures (CAPEX) as well as operating expenditures (OPEX) due to lower heating budget and longer life. In fact, once the operating temperature is reduced below 250 °C, the conventional polymer sealing and electrical insulation technologies can be used. Besides, the heat dissipation will also be dramatically reduced when the operating temperature is lowered below 250 °C, because the radiant heat

* Corresponding author.
** Corresponding author.
E-mail addresses: xiaohuining@mail.xjtu.edu.cn (X. Ning), liju@mit.edu (J. Li).

https://doi.org/10.1016/j.ensm.2019.09.008
Received 14 April 2019; Received in revised form 30 August 2019; Accepted 2 September 2019
Available online xxxx

Please cite this article as: T. Dai et al., A low-cost intermediate temperature Fe/Graphite battery for grid-scale energy storage, Energy Storage Materials, https://doi.org/10.1016/j.ensm.2019.09.008

transfer (the main heat transfer mode at very high temperature) is proportional to temperature to the fourth order, and the other two heat transfer modes (conduction and convection) can be easily blocked by vacuum insulation at the 'intermediate' temperature range. More importantly, compared with the room temperature batteries, the intermediate-temperature batteries still retain the enhanced rate performances (quickened kinetics) endowed by the relatively higher operating temperature, which is of great significance in the context of grid scale energy storage applications.

In this context, it was noted that amongst molten salts, tetrachloroaluminate melts have very low melting temperatures due to the size mismatch of the large $AlCl_4^-$ anion with the small metal cations, that destabilizes crystalline packing thermodynamically [18]. Specifically, $NaAlCl_4$, which has a melting point of 157 °C, can potentially be used as an electrolyte for intermediate-temperature batteries. This electrolyte is produced by reacting NaCl with $AlCl_3$ and their binary phase diagram is shown in Fig. S1. We will use this liquid electrolyte in the NaCl-saturated regime, where $NaAlCl_4$(liq) + NaCl(solid) coexist. The excess NaCl(solid) particles get evenly distributed while some appear to be on or near the anode surface.

Usually with a metallic anode, long-range diffusional instabilities in the electrolyte can drive the formation of dendrites, which is a safety concern. The growth of dendrites corresponds to a metal deposition process, facilitated by the presence of free cations and anions in the electrolyte which are released/received across a long distance, reflected by the Sand's extinction and limiting current [19–25]. This long-range transport instability can be suppressed if an Fe(solid)/$FeCl_2$(solid) electrode couple is employed as the anode in the presence of widely available excess NaCl(solid). $FeCl_2$, which is produced when Fe electrode oxidizes, is almost insoluble in the NaCl-saturated molten $NaAlCl_4$ electrolyte (the solubility of $FeCl_2$ in $NaAlCl_4$ melt is 3.79×10^{-5} mol% at 175 °C) [26,27]. Thus upon oxidation, instead of Fe^{2+}(electrolyte), two Na^+(electrolyte) are released into the electrolyte after some NaCl(solid) nearby contributes the two chlorine ions. Upon reduction, the reverse happens. Since the Fe^{2+} ions are completely arrested in the above-mentioned process and finite ionic strength is guaranteed at the solid-liquid interface, no Sand's singularity and no Fe dendrites can be formed on the anode [25]. There is also no buildup of solid-electrolyte interphase (SEI), as the anode is operated within the electrochemical stability window of the molten salt electrolyte. Although the Fe/$FeCl_2$ couple –owing to its high electronegativity– has traditionally been used as a cathode in ZEBRA type batteries, there is a clear advantage in using it as an anode in this particular situation [28].

Similarly, a suitable cathode, which can be used in conjunction with the $NaAlCl_4$ electrolyte, has to be identified. In 2015, Lin et al. designed an ultrafast aluminum-ion battery possessing high rate capability and long cycle life [29]. Their battery uses a non-flammable organic ionic liquid electrolyte and operates via the electrochemical deposition and dissolution of Al at the anode, and intercalation/de-intercalation of chloroaluminate anions ($AlCl_4^-$) at a graphite cathode [30–32]. Notably, it was observed that the graphite cathode exhibits high rate capability and stability while undergoing $AlCl_4^-$ intercalation and de-intercalation [33,34].

Motivated by this, we chose graphite as the cathode and assembled an 'Fe/$NaAlCl_4$/Graphite' battery with excess NaCl(solid) that operates at 170 °C. This cell has a round-trip Coulombic efficiency of 99.5% and exhibits a capacity retention rate of over 85%, even after being subjected to nearly 10,000 charge-discharge cycles. Owing to the highly reversible solid to solid transition between Fe and $FeCl_2$, undesirable dendritic growth of Fe on the anode is prevented. On further optimizing the balance of consumption of the two electrode capacities and electrolyte, it was determined that the battery can be overcharged without any safety problems. Given that this battery consists of inexpensive components, it has the potential to meet demands for large scale and cost-effective grid-scale energy storage solutions.

2. Material and methods

2.1. Electrolyte synthesis

The NaCl saturated $NaAlCl_4$ electrolyte was prepared by mixing and heating anhydrous NaCl (99.99%, Aladdin) and anhydrous $AlCl_3$ (99%, Aladdin) together at 200 °C. To ensure that the solution is saturated with NaCl, the molar ratio of NaCl and $AlCl_3$ was adjusted to a value slightly greater than 1. Saturation is confirmed when some solid NaCl residue precipitates out after the mixture becomes liquid. Initially, the freshly produced molten $NaAlCl_4$ is brown in color due to the presence of impurities like $Fe^{2+}$and Zn^{2+}. After adding small quantities of Al debris to the molten $NaAlCl_4$ and letting it stand overnight, the mixture becomes colorless. Additionally, moisture is eliminated by stewing the molten $NaAlCl_4$ at elevated temperatures [35]. All the processes mentioned above were conducted in an Ar-filled glove box.

2.2. Preparation of Fe/$FeCl_2$ electrode

Whenever $FeCl_2$ reversibly transforms to Fe in the cell, the active anode material can potentially detach from the current collector. Therefore, proper adhesion has to be maintained between the $FeCl_2$ anode and the Fe-metal current collector. In view of this, we developed a fabrication method wherein a $FeCl_2$/Fe electrode with a certain capacity could be obtained by exposing Fe to HCl gas. Also, by the varying the exposure time, the size of $FeCl_2$ particles can be easily controlled.

A piece of high purity Fe metal (plate or foam, 99.999%, Aladdin), is suspended over a pool of concentrated hydrochloric acid and stored inside a sealed container. After some time, the Fe piece gets corroded by HCl gas, and a thin layer of $FeCl_2$ forms on its surface. Following this, the Fe piece is taken out from the sealed container and dried at 200 °C in Ar atmosphere for one night. Since the residual HCl gas and moisture on the Fe surface evaporate on drying, the mass of Cl can be determined by comparing the change in the mass of Fe, before and after the treatment. In addition to $FeCl_2$, this treatment can also potentially produce a certain amount of $FeCl_3$. Therefore, an Fe/$FeCl_2$ electrode prepared by this method was examined by XRD to determine its composition. From the XRD scan shown in Fig. S7, only peaks corresponding to Fe and $FeCl_2$ are observed, which confirms that no $FeCl_3$ was produced on the electrode. Regardless, formation of $FeCl_3$ would not have caused serious concern anyway because all of it transforms to $FeCl_2$ in the presence of Fe, when the cell is in operation. Note that the theoretical capacity of Fe/$FeCl_2$ anode is defined in this paper with respect to the mass of $FeCl_2$.

2.3. Preparation of Mo/$FeCl_2$ electrode

A $FeCl_2$ saturated ethanol solution is evenly dripped on the surface of a Mo plate using a transfer pipette such that it has an areal density of 17.7 μl cm^{-2}. Thereafter, the Mo plate is dried at 200 °C in Ar atmosphere for 1 h. After drying, the Mo/$FeCl_2$ electrode, which consists of a smooth layer of $FeCl_2$ tightly attached to the Mo plate, is created.

2.4. Anode characterization

To observe the surfaces of the prepared Mo/$FeCl_2$ and Fe/$FeCl_2$ electrodes before charging, they both were directly transferred to the sample compartment of a field emission scanning electron microscope (SEM, Hitachi SU6600) from the Ar-filled glove box. Energy-dispersive X-ray spectroscopy (EDS, EDAX) was used to map the distribution of different elements.

Prior to characterizing charged Fe/$FeCl_2$ anodes with SEM, EDS and XRD, certain pre-treatments were performed on them. In order to observe the morphology of Fe particles on a charged Fe/$FeCl_2$ electrode, the latter was cooled to room temperature after charging and ultrasonically treating it in deionized water to remove any adhering salt.

On the other hand, the charged Mo/$FeCl_2$ plate anode was scratched

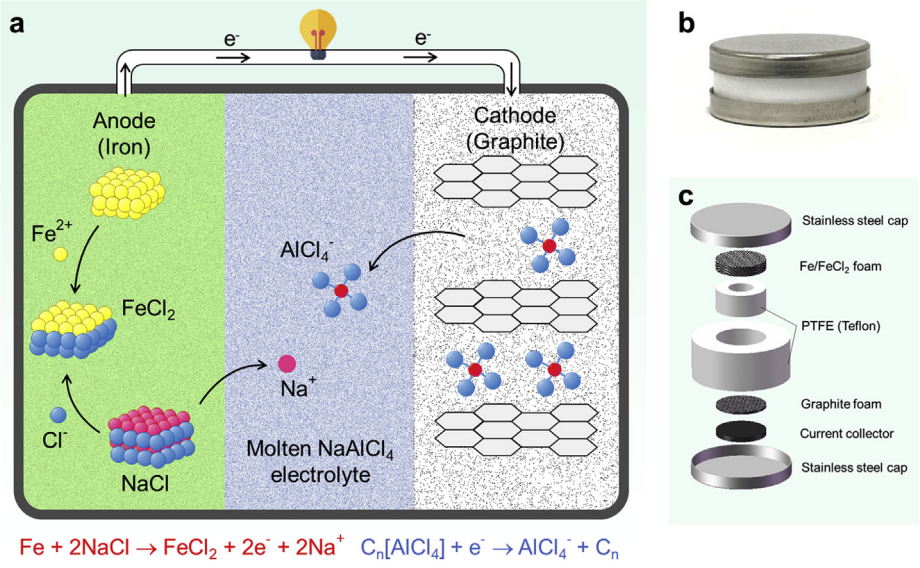

Fig. 1. (a) Schematic illustration of the Fe/graphite cell during discharge. (b) A view of a fully assembled home-made Fe/graphite cell with a diameter of 2 cm. (c) An exploded view of the home-made Fe/graphite cell.

by a blade to locally remove the attached $NaAlCl_4$ layer so that the material underneath is exposed.

Furthermore, the fully charged cell with a Mo/$FeCl_2$ plate anode was cooled to room temperature. Then the Mo/$FeCl_2$ plate anode was removed from the cell and heated at 300 °C for 2 h to evaporate and eliminate the $NaAlCl_4$ layer. Following this, the active materials were scraped off the Mo plate. To avoid contamination from air/moisture in the ambient atmosphere, the active materials were placed onto a glass slide and wrapped by Scotch tape. The wrapped sample was immediately removed from the glove box and transferred to a PANalytical X'pert Pro diffractometer for performing XRD measurements.

2.5. Cathode characterization

First, both primitive and charged graphite were ground into microscopic particles and dispersed in acetone by ultrasonic agitation. Next, this dispersion was dripped over a micrograte. Once the acetone volatilizes, the graphite particles on the micrograte were transferred into the sample chamber of high resolution transmission electron microscopy (HRTEM, JEOL 2100F). The thin edges of the graphite particles were characterized in high resolution mode and the elemental distribution of graphite particles was determined by energy-dispersive X-ray spectroscopy in HRTEM (EDS, JEOL).

2.6. The cyclic voltammetry (CV) test

Al plates with active areas of 1 cm^2 and 5 cm^2 were used as the reference electrode and counter electrode, respectively. Molten $NaAlCl_4$ saturated with NaCl is employed as the electrolyte and the setup was operated at 170 °C. Fe/$FeCl_2$ (active area, 0.7 cm^2; CV scan rate, 0.01 V/s) and a graphite composite electrode (active area, 2 cm^2; CV scan rate, 0.001 V/s) were the working electrodes. The following procedure was adopted to prepare the graphite composite electrode. First, natural graphite flakes (obtained from Aladdin) were ground into micro-sized particles and dispersed uniformly on a carbon fiber cloth (CeTech Co., Ltd.) with the assistance of acetone. The areal density of the dispersion was about 0.7 mg cm^{-2}, which was same as that of the previously mentioned graphite particles on a micrograte. Thereafter, this carbon fiber cloth was sandwiched between two layers of glass fiber filter paper (Whatman GF/A). Finally, the sandwich structure was rolled into a cylinder, and the carbon fiber cloth was exposed as the electrical lead. All processes were conducted in Ar-filled glove box, and the cyclic voltammetry tests were performed on an electrochemical workstation (CHI660E, Chenhua).

2.7. Cell structure and testing

Cells were assembled by home-made cell shells, which have the active area of 0.2 cm^2. The anode and cathode were separated by a PTFE washer, which was then deformed under the pressure to seal the cell. The traditional 2032 coin cell shell and a piece of glass carbon were used as current collectors. (shown in Fig. 1 (b) and (c)).

The galvanostatic charge-discharge performance tests were performed with a battery tester (BT2000, Arbin).

2.8. The electrode materials

The graphite foam (GF) was purchased from *Six Carbon Technology* (Shenzhen, China). It is prepared by growing graphite layers on nickel foam scaffold templates via chemical vapor deposition (CVD). Following this, the nickel foam is dissolved in $FeCl_3$ solution and the GF residue is dried in Ar atmosphere.

The graphite powder (GP) cathode is fabricated by rolling out the mixture of artificial graphite powder (D50 8–10 um; 90 wt%) and polytetrafluoroethylene (10 wt%) into thin films and drying at 120 °C in vacuum for 8 h.

The Fe/$FeCl_2$ plate (FP) anode, Fe/$FeCl_2$ foam (FF) anode, the GF cathode and the GP cathode used in the cells are shown in Fig. S8 (a), (b), (c) and (d).

Also, the microstructural features of the GF, graphite cloth, GP and the as-prepared FF can be seen in Fig. S9 (a), (b), (c) and (d).

3. Results and discussion

3.1. Cell assembly and reactions

The cell is assembled in the fully discharged state, consisting of a graphite cathode C_n, NaCl-saturated molten $NaAlCl_4$ electrolyte, and an anode with Fe backbone as the current collector with $FeCl_2$ particles dispersed on its surface. Upon charging at a temperature of 170 °C, the cathode voltage increases (oxidation) while the anode voltage decreases (reduction), with the following reactions:

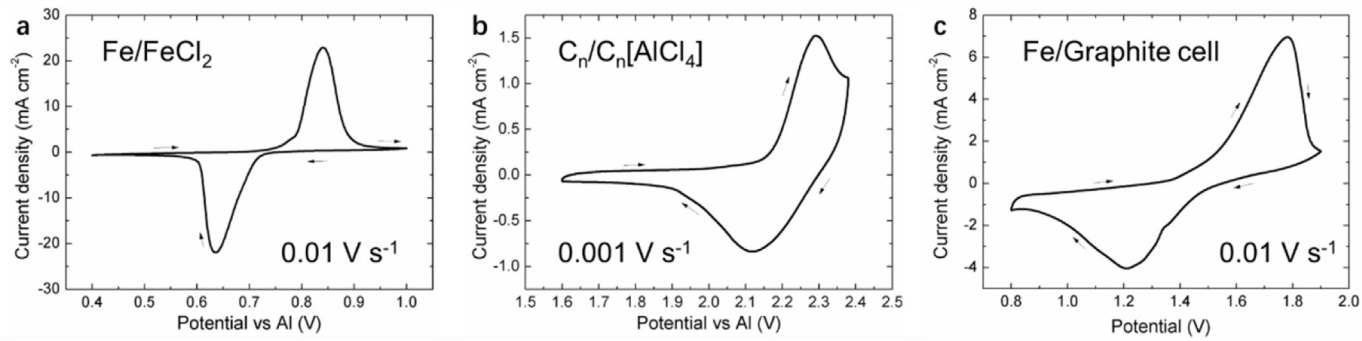

Fig. 2. Cyclic voltammetry (CV) tests. (a) The CV curve of $Fe/FeCl_2$ obtained in the three-electrode cell with the Al reference electrode, Al counter electrode and the molten NaCl saturated $NaAlCl_4$ electrolyte at 170 °C. (b) The CV curve of the graphite electrode ($C_n/C_n[AlCl_4]$) in the same three-electrode cell at 170 °C. (c) The CV curve of a two-electrode Fe/Graphite cell at 170 °C.

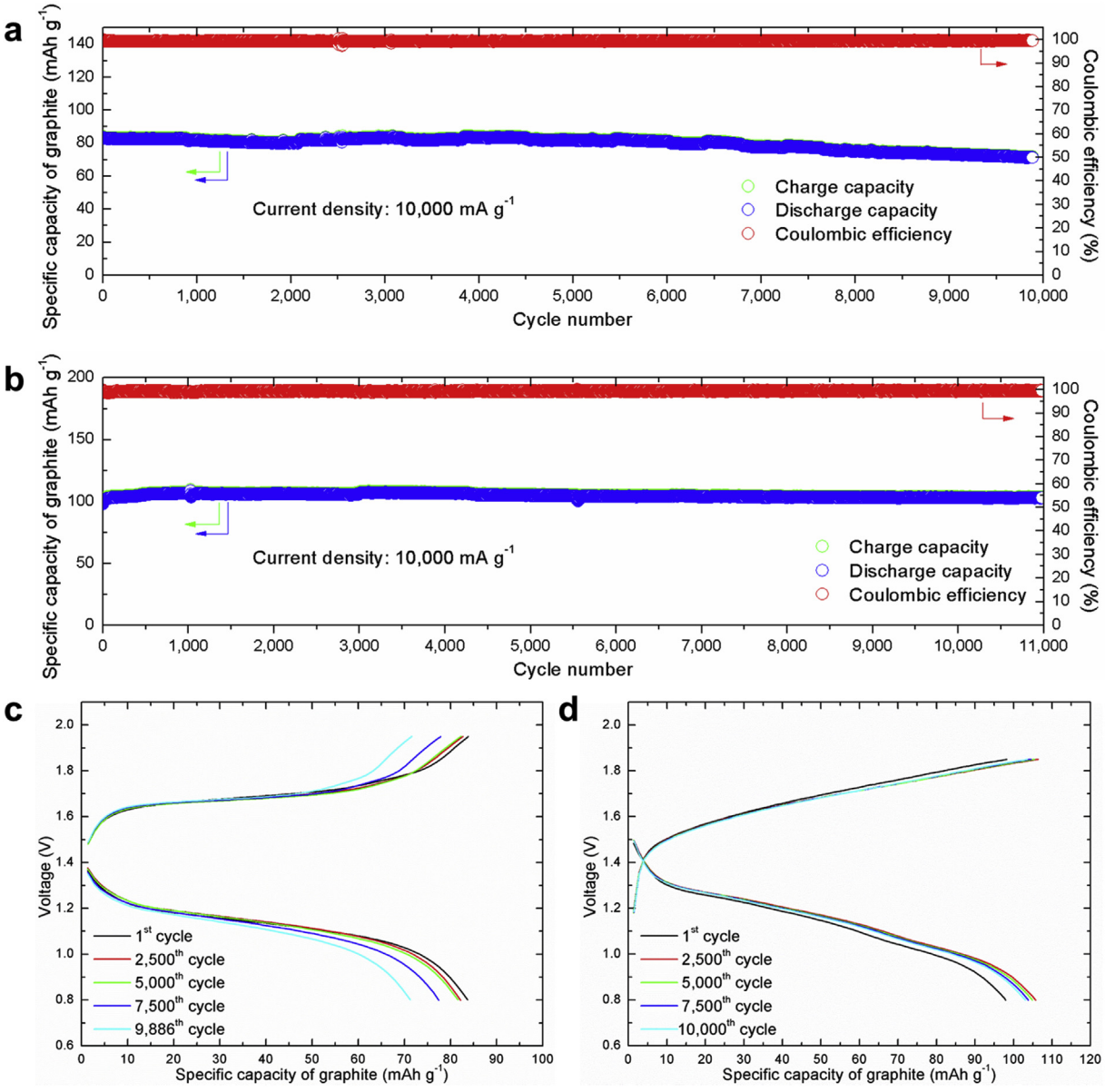

Fig. 3. The cycling performance and voltage curves of two Fe/Graphite cells with different electrode capacity matching strategies. (a) The cycling performance of the Fe/Graphite cell with an $Fe/FeCl_2$ plate (FP) anode and a graphite foam (GF) cathode at the current density of 10,000 mA g^{-1} for graphite. (b) The cycling performance of the Fe/Graphite cell with $Fe/FeCl_2$ foam (FF) anode and a GF cathode at the same current density of 10,000 mA g^{-1} for graphite. (c) The voltage curves of the FP-GF cell at different cycles. (d) The voltage curves of the FF-GF cell at different cycles.

Cathode voltage ↑: $C_n + AlCl_4^-(electrolyte) \rightarrow C_n[AlCl_4] + e^-$ (1)

Anode voltage down ↓: $FeCl_2 + 2e^- + 2Na^+(electrolyte) \rightarrow Fe + 2NaCl$ (2)

The $NaAlCl_4$(liq) electrolyte is thus being consumed in charging, and new NaCl(solid) will be formed. The high ionic strength of $NaAlCl_4$(liq) and the broad availability of $FeCl_2$(solid) prevent any transport-limited morphological instabilities [25]. In principle, for the battery to work, pure $NaAlCl_4$ (liq) electrolyte should do fine. However, because NaCl(-solid) is a key intermediary and source of chlorine or sodium ions, it is safer to have $NaAlCl_4$ (liq) + NaCl(solid) electrolyte with a slight NaCl-excess initially.

In the fully charged state, all the $FeCl_2$ would have been reduced to Fe (the best arrangement turns out to be having the battery run in the anode-limited mode, with capacity given by the initial amount of anode-bound $FeCl_2$, as we will discuss later), and the graphite C_n would have been oxidized to form the $AlCl_4^-$ intercalated graphite $C_n[AlCl_4]$. Upon discharging, the following cathode reduction and anode oxidation reactions occur:

Cathode voltage ↓: $C_n[AlCl_4] + e^- \leftrightarrow AlCl_4^-(electrolyte) + C_n$ (3)

Anode Voltage ↑: $Fe + 2NaCl \leftrightarrow FeCl_2 + 2e^- + 2Na^+(electrolyte)$ (4)

where Fe oxidizes, but because of Fe^{2+}'s insolubility, combines with Cl^- ions (supplied by NaCl) to electrodeposit solid $FeCl_2$, with a net ejection of Na^+(electrolyte) from the anode side. We note that Cl^- ions are in a dynamic flux inside the liquid electrolyte (exchanges between $AlCl_4^-$(electrolyte) and NaCl(solid) in Grotthuss diffusion mechanism), thus there is no need for the NaCl(solid) to be too close or even in contact with the current collector, as long as there is a net excess of NaCl(solid) in some region near where the iron oxidation happens. A schematic illustration of the discharging mechanism is shown in Fig. 1 (a). We note that because the electrolyte mixture $NaAlCl_4$ (liq) + NaCl(solid) actively participate in the reactions on both electrodes, balance of plant would require the masses of the initial $FeCl_2$, C_n, and $NaAlCl_4$ (liq) to satisfy some inequalities, to be detailed later.

Since the cell operates at 170 °C, low-cost polymers like PTFE can be used to seal it, and there is less corrosion and heat insulation problems, which reduce the CAPEX as well as OPEX of the battery, improving the system's total energy efficiency greatly [13]. An assembled home-made cell along with its individual components are displayed in Fig. 1 (b) and (c).

3.2. Characterization of electrochemical properties

3.2.1. Cyclic voltammetry

Cyclic voltammetry tests, using a three-electrode system, were conducted on $Fe/FeCl_2$ and $C_n/C_n[AlCl_4]$ electrodes to evaluate their electrochemical performances.

The individual cyclic voltammograms (CV) of the $Fe/FeCl_2$ and $C_n/C_n[AlCl_4]$ electrodes in a NaCl-saturated molten $NaAlCl_4$ electrolyte, at 170 °C, are displayed in Fig. 2 (a) and (b), respectively. In both figures, a distinct redox peak couple can be identified. From the position of these redox peak couples, the corresponding equilibrium potentials, U_{anode} and $U_{cathode}$, of the $Fe/FeCl_2$ and $C_n/C_n[AlCl_4]$ electrodes are roughly 0.74V and 2.18V, respectively. So, the open circuit voltage (OCV) of the $Fe/FeCl_2/NaAlCl_4/C_n[AlCl_4]/C_n$ cell can be inferred to be about 1.44V.

Similarly, the result of cyclic voltammetry test conducted on a two-electrode Fe/Graphite full-cell is shown in Fig. 2 (c). Much like the previously tested electrodes, well defined oxidation and reduction peaks, appear at 1.78 V and 1.21 V, respectively. Positions of the two redox peaks are consistent with the inferred value of OCV for the Fe/Graphite cell.

3.2.2. Galvanostatic charge/discharge performance

Cycling performance of the Fe/Graphite battery full-cell, which contains an $Fe/FeCl_2$ plate (FP) anode and graphite foam (GF) cathode, was further evaluated by charging and discharging for nearly 10,000 cycles at a current density of 10,000 mA g^{-1} for graphite (this FP-GF battery was also cycled at current densities ranging from 3333 to 10,000 mA g^{-1}, and the rate performance can be seen in Fig. S2). Variations in the specific capacity of GF, measured at a current density of 10,000 mA g^{-1}, are displayed in Fig. 3 (a). Note that the capacity retention rate, after nearly 10,000 cycles, is higher than 85%. This amounts to a capacity decay rate of only 0.0015% per cycle, demonstrating excellent stability. To further assess the cyclic stability, the voltage curves at different stages of charging and discharging are compared in Fig. 3 (c). As can be seen from this figure, each voltage curve exhibits a clear and steady plateau during charging and discharging. At the end of each charge and discharge cycle, there is a sharp rise and drop in the voltage, respectively. This aspect will be discussed in detail later. Beyond 5000 cycles, while the discharge specific capacity reduces gradually, the plateau potentials of charge and discharge curves remain invariant. The invariance in the plateau potentials attests to the highly reversible nature of electrode reactions and the stability of their electrochemical polarization.

Additionally, in this battery, the initial specific capacity of GF cathode is ~84 mAh g^{-1}, the Coulombic efficiency is 99.5% (See Fig. 3 (a)) and the charge/discharge rate is as high as ~120C, when the current density at the FP anode reaches ~7.5 mA cm^{-2}.

Interestingly, both the CV curve of graphite in Fig. 2 (b) and the charge and discharge voltage curves in Fig. 3 (c) show that there is only one electrochemical reaction on the graphite cathode side in the Fe/Graphite cell, which should correspond to one voltage plateau on charging or discharging. However, in the Al/Graphite battery, immense amounts of previous studies have demonstrated two distinct voltage plateaus corresponding to two electrochemical reactions on the graphite cathode side [29,30,33,34,36,37]. Dai et al. claimed that these two distinct voltage plateaus actually correspond to the intercalation of $AlCl_4^-$ into graphite with 2 stages during charging in an $AlCl_3$-urea ionic liquid, while in the $NaAlCl_4$ molten salt electrolyte, Jiao et al. proposed that there are two kinds of anions ($AlCl_4^-$ and $Al_2Cl_7^-$) co-intercalate into the graphite that correspond to two distinct voltage plateaus respectively [33,34]. Here, through the comparison of graphite cathodes in the Al/Graphite cell and the Fe/Graphite cell, we get another unique angle of view on the meaning of the two voltage plateaus.

For the reactions on the graphite side, there is a key difference (depending on the acid-base property of the electrolyte) between Al/Graphite cell and Fe/Graphite cell. The Fe/Graphite cell uses a basic $NaAlCl_4$ electrolyte ($NaCl/AlCl_3$ mole ratio ≥ 1), while the Al/Graphite cell needs to be operated with an acidic $XAlCl_4$ electrolyte ($XCl/AlCl_3$ mole ratio < 1, X can be alkali metal cations or organic cations, like $NaAlCl_4$ molten salt or $AlCl_3$/[EMIm]Cl ionic liquid) to ensure high quality aluminum deposition [29,34,38,39]. In the basic $NaAlCl_4$ electrolyte of Fe/Graphite cell, $AlCl_4^-$ (basic as Cl^- donor) serves as the anions, and the intercalated ions in graphite should be $AlCl_4^-$. However, the $AlCl_4^-$ and $Al_2Cl_7^-$ (acidic as Cl^- acceptor) both exist as anions in the acidic $XAlCl_4$ electrolyte of Al/Graphite cell. As a consequence, it can be deduced that in the Al/graphite cell, apart from one voltage plateau corresponding to the intercalation of $AlCl_4^-$ into graphite, the other voltage plateau should be related to the reaction with $Al_2Cl_7^-$ anions.

To further improve the capacity retention rate, which is critical for grid-scale energy storage, it is important to determine which of the two electrodes contributes more to the overall cell capacity decay rate. Typically, if the graphite electrode's capacity is in excess, capacity fading of the cell during cycling would originate from the damage accumulated on $Fe/FeCl_2$ side, and vice versa.

Hence, another Fe/Graphite cell was assembled using the $Fe/FeCl_2$ foam (FF) anode instead of the FP anode. The FF anode in this cell is

expected to have excessive capacity on account of possessing ~30 times higher active surface area and $FeCl_2$ content than that of the original FP anode.

This FF-GF cell was also cyclically charged and discharged for over 10,000 times at a constant current density of 10,000 mA g^{-1}. Fig. 3 (b) and (d) display its cycling data and voltage curves at different stages of charging and discharging, respectively. As can be seen, the average specific capacity of the GF cathode is ~104 mAh g^{-1} and the Coulombic efficiency is 99.3%. In addition, it has an extremely low capacity fade rate of 0.00034% per cycle. Note that the specific capacity of GF in this FF-GF cell is 20 mAh g^{-1} higher than that in the FP-GF cell. This confirms that in the FP-GF cell, the GF cathode's reported specific capacity was actually underutilized and hence the GF cathode was in excess. Alternately, in the FF-GF cell, the FF anode would have excess capacity. It then follows that the higher capacity fade rate per cycle of the FP-GF cell, which is 0.0015%, represents the cycling performance of the FP anode. Because 0.0015% per cycle is more than quadruple of 0.00034% per cycle, it means a full cell with FP anode would see its long-term cycling performance limited by the anode.

The FP-GF cell and the FF-GF cell will hitherto be alternatively referred as graphite-excess and $FeCl_2$-excess cells, respectively. On comparing the voltage curves of these two cells, an additional difference can be noted. While the voltage of the former increases sharply at the end of charging, such a feature is absent in the latter (see Fig. 3 (c) and (d)). The discharging segments of both the cells are, however, similar in nature. To address this peculiarity in the charging curves of the graphite-excess cell, the underlying mechanism of each capacity matching strategy must be understood.

Before that, it is important to know the specific capacities of both electrodes. The theoretical specific capacity of the $Fe/FeCl_2$ electrodes can be calculated as 2*e* divided by the mass of $FeCl_2$, which is 423 mAh g^{-1}. However, the maximum reversible specific capacity of the graphite electrode is still unknown (which depends on the quality and quantity of graphitization). For measuring this, the $FeCl_2$-excess cell was cycled with different charging cutoff capacities ranging from 500 mAh g^{-1} to 104 mAh g^{-1} per graphite mass. The corresponding charge and discharge voltage curves are presented in Fig. S3 (a). At a current density of 10,000 mA g^{-1}, a new charge voltage plateau at about 2.0 V emerges together with a new discharge voltage plateau arising at about 1.45V. As the charging cutoff capacity is reduced, both voltage plateaus gradually diminish. This is accompanied by a simultaneous increase in the Coulombic efficiency from 65.66% to 99.04%. Finally, when the cut-off capacity is reduced to 104 mAh g^{-1} (cut-off voltage of 1.85V), the new voltage plateaus (about 2.0 V in charge, and about 1.45V in discharge) completely disappear. It is speculated that the charging (discharging) voltage plateaus correspond to the production (reduction) of Cl_2 gas [40,41]:

$$\text{Cathode voltage}\uparrow\text{: } 2AlCl_4^-(\text{electrolyte}) \rightarrow 2AlCl_3(\text{solid or gas}) + Cl_2(\text{gas}) + 2e^- \quad (5)$$

a side reaction in reference to (1). Cl_2(gas) is corrosive and highly undesirable. This reaction happens when there is excess anode $FeCl_2$, and when the cell is charged beyond the cathode reversible capacity [29,34]. Hence, the cut-off capacity at which these plateaus disappear can be regarded as the maximum reversible specific capacity of graphite. According to this criterion, the maximum specific capacity of our graphite, at the current density of 10,000 mA g^{-1}, is 104 mAh g^{-1}. Besides, the higher discharge capacities and the higher voltage plateaus can be attributed to the partial reduction of Cl_2 on the surface of graphite.

To further understand the mechanisms of charging and discharging, the CV curve of the $C_n/C_n[AlCl_4]$ electrode, measured at the sweep speed of 0.05 V s^{-1}, is displayed in Fig. S3 (b). In the oxidation segment of the curve, the intercalation peak of $AlCl_4^-$ partially overlaps with the peak corresponding to the formation of Cl_2. This was not observed in the CV curves shown in Fig. 2 (b) because slower sweep speeds can separate the two peaks. Nevertheless, the relative proximity of the two peaks indicates that the intercalation potential of $AlCl_4^-$ in graphite is close (~0.2V) to the potential at which Cl_2 is produced.

Next, to assess the performance of different electrode capacity matching strategies, in Fig. S3 (c) the four electrodes, $Al/AlCl_4^-$, $Fe/FeCl_2$, $C_n/C_n[AlCl_4]$ and $AlCl_4^-/Cl_2$, are arranged in the ascending order, from left to right, according to their corresponding equilibrium potentials [15]. The potential window of the NaCl-saturated $NaAlCl_4$ electrolyte lies between the potentials of $Al/AlCl_4^-$ and $AlCl_4^-/Cl_2$ [40]. Using this schematic, the operating mechanisms for different types of electrode capacity matching strategies can be deduced in any Fe/Graphite batteries, which use NaCl-saturated $NaAlCl_4$ electrolyte along with $Fe/FeCl_2$ and $C_n/C_n[AlCl_4]$ electrodes. For instance, in a graphite-excess cell, Al is deposited on the anode if the cell is slightly overcharged:

$$\text{Anode voltage down}\downarrow\text{: } AlCl_4^-(\text{electrolyte}) + 3e^- + 4Na^+ \rightarrow Al(\text{solid}) + 4NaCl \quad (6)$$

a side reaction in reference to (2). An alternative way to rewrite (6) is to add the chloro-exchange reaction:

$$4Al_2Cl_7^-(\text{electrolyte}) + 4NaCl = 8AlCl_4^-(\text{electrolyte}) + 4Na^+$$

that is constantly occurring inside the electrolyte irrespective of electrode voltage (the chloro-acid/chloro-base equilibrium), to give

$$\text{Anode voltage down}\downarrow\text{: } 4Al_2Cl_7^-(\text{electrolyte}) + 3e^- \rightarrow Al(\text{solid}) + 7AlCl_4^-(\text{electrolyte}) \quad (6')$$

This reaction (6) or (6′) is much more benign compared to (5). Contrasting (6), (6′) with (5) has great implications in the context of choosing an appropriate electrode capacity matching strategy for the Fe/Graphite cell. Considering that the formation of Cl_2 gas during overcharging is perhaps dangerous, whereas side reaction (6) is quite benign, the graphite electrode in the cell should possess higher capacity than the $FeCl_2$ electrode. Such an electrode capacity matching strategy for full-cell is optimal in the event of overcharging as the excessive capacity of graphite will function as the reserve capacity.

A typical overcharge voltage curve of the graphite-excess cell is shown in Fig. S3 (d). The charging voltage curve rises abruptly from 1.7 to 1.95 V when the $FeCl_2$ is exhausted, and then the Al deposition process emerges; only after the reserve capacity of graphite is used up can Cl_2 (gas) be produced. Compared with the graphite-excess cell, the $FeCl_2$-excess cell has no abrupt voltage rise before Cl_2 formation when overcharged, as seen in Fig. S3 (a). From the schematic shown in Fig. S3 (c), this phenomenon can be attributed to the larger potential difference between the $Al/AlCl_4^-$ and $Fe/FeCl_2$ electrode pairs (~0.74V, see Fig. 2 (a)) in the graphite-excess cell than that between $C_n/C_n[AlCl_4]$ and $AlCl_4^-/Cl_2$ (~0.2V, see Fig. S3 (b)) in the $FeCl_2$-excess cell [26,40].

Note that the voltage excursion at the end of charging is vitally important for the battery management system (BMS), because the BMS usually needs a trigger signal of cell voltage change at the end of charging. In this sense, the graphite-excess cell is much more desirable for the design and operation of BMS for grid-scale energy storage.

Consequently, the slightly graphite-excess cell provides the optimal electrode capacity matching strategy, not only because it reduces the risk of Cl_2 production in the event of overcharging, but also because the voltage excursion at the end of charging guarantees the smooth operation of BMS.

Additionally, from another perspective, it can also be seen from Fig. S3 (c) that the Fe/graphite cell actually sacrifices the voltage between $Al/AlCl_4^-$ and $Fe/FeCl_2$ electrode pairs, compared with the Al/Graphite cell (if the difference on the acid-base property of electrolytes is not considered). But it is the unutilized voltage range between $Al/AlCl_4^-$ and $Fe/FeCl_2$ electrode pairs that eliminates the risk of Cl_2 production in the event of overcharging with the help of the graphite-excess electrode capacity matching strategy. In contrast, the Al/Graphite cell almost utilizes the entire range of potential window of tetrachloroaluminate melts,

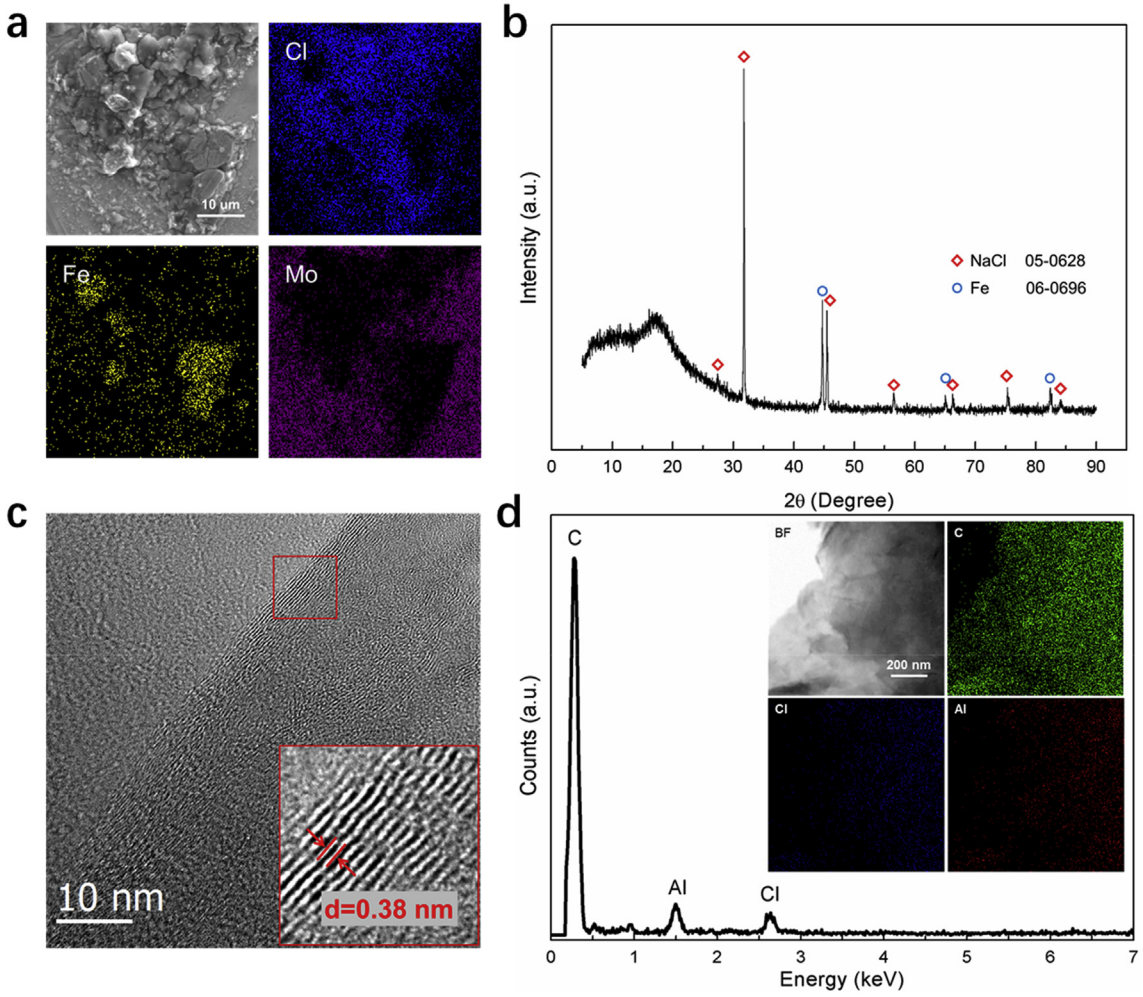

Fig. 4. Characterization of electrodes in the Fe/Graphite battery. (a) The micromorphology and elemental mapping of the Mo/$FeCl_2$ anode plate in the fully charged state. (b) The XRD data of the active materials on the Mo/$FeCl_2$ anode plate in the fully charged state. (c) The HRTEM image of a particle extracted from the graphite electrode after charging. The interplanar distance of (002) of fully charged graphite is ~0.38 nm. (d) The elemental mapping and the compositional profile of the charged graphite particle acquired by EDS in TEM.

except the range between $C_n/C_n[AlCl_4]$ and $AlCl_4^-/Cl_2$ (~0.2V). Thus, when the cell is slightly overcharging, the Cl_2 gas would be produced on the cathode side, which is corrosive and possibly disastrous for grid-scale battery energy storage [29,33].

3.3. Mechanism confirmation

In order to investigate the morphology of Fe metal during charging, an ethanol solution containing $FeCl_2$ was evenly dripped on a Mo foil and dried in Ar. Fig. S4 (a) shows the elemental distribution of the resulting thin layer of $FeCl_2$ formed on the inert Mo foil. Thereafter, using this Mo/$FeCl_2$ composite plate as an anode, a cell was assembled. After the first charging, the cell was cooled to the room temperature and the $NaAlCl_4$ layer on the anode plate was locally removed. The micromorphology and elemental distribution of the Mo/$FeCl_2$ anode plate in the fully charged state is shown in Fig. 4 (a). Since Fe metal particles appear to have formed on the plate, our hypothesis that $FeCl_2$ transforms to Fe is confirmed. To verify that the deposited particles are pure Fe, the active materials of the fully charged anode were scraped off from the Mo substrate and tested with XRD. As expected, peaks corresponding to elemental BCC Fe were observed in the XRD scans and can be seen in Fig. 4 (b). Note that before performing XRD tests, $NaAlCl_4$ was evaporated and removed from the fully charged anode plate by heating it at 450 °C in Ar for 4 h [42]. The same procedure was adopted before characterizing the active materials on the anode plate, in the fully discharged state. The results of the XRD tests, summarized in Fig. S4 (b), also confirm the existence of $FeCl_2$ in the fully discharged anode. From these observations it is conclusively established that Fe and $FeCl_2$ form reversibly during charging and discharging, respectively.

After being fully charged, the graphite cathode was ground to submicron-sized particles and characterized by HRTEM. The HRTEM image of the fully charged graphite particle is displayed in Fig. 4 (c). To facilitate comparison, the HRTEM image of a graphite particle in the pristine state (or pre-charged state) is shown in Fig. S5. From these images it can be observed that the interplanar distance of (002) planes in graphite increases from 0.34 nm to ~0.38 nm on charging.

Next, using EDS in the TEM, the elemental distribution of fully charged graphite particles was determined, as shown in Fig. 4 (d). It is revealed that Cl and Al are uniformly distributed within the fully charged graphite. The presence of these two elements could also results from the molten electrolyte not being fully removed from the graphite electrode surface. However, since Na is absent in the elemental map, we can confirm that Al and Cl are indeed absorbed into graphite as $C_n[AlCl_4]$ and the above stated results have not been influenced by preparation artifacts.

Since the Cl and Al elements are confirmed to be distributed within the fully charged graphite and the interplanar distance of (002) planes in graphite increases after charging, we can conclude that the Cl and Al

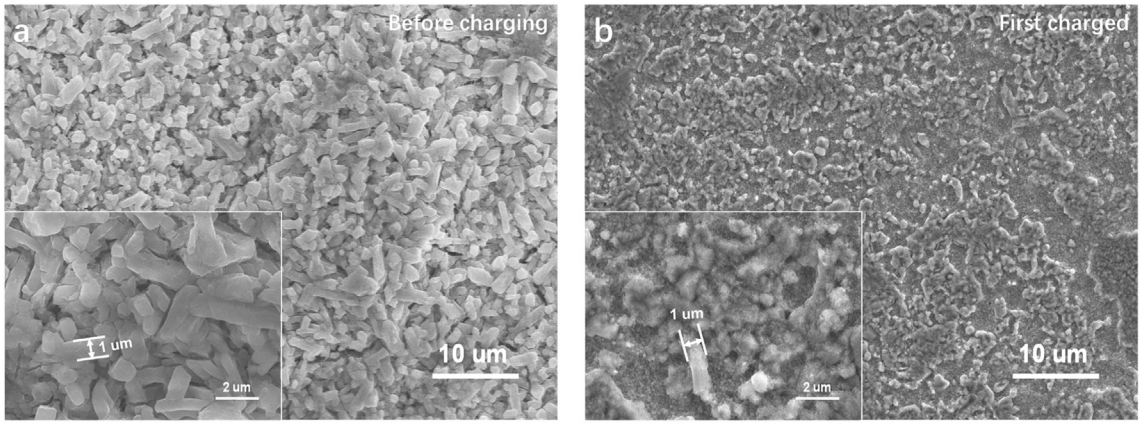

Fig. 5. The morphological evolution of Fe and $FeCl_2$ particles. (a) Rod-like $FeCl_2$ particles on the Fe/$FeCl_2$ plate electrode before charging. (b) Flocculated Fe particles on the anode plate after the first charge.

elements are intercalated in the form of $AlCl_4^-$ into graphite on charging, which had also been demonstrated and studied by Dai et al. and Jiao et al. before [29,33,34].

As mentioned before, there are almost no free Fe^{2+} ions in the molten NaCl saturated $NaAlCl_4$ electrolyte due to the low solubility of $FeCl_2$ in it. As a matter of fact, the amount of $FeCl_2$ dissolved in the electrolyte is less than 1/100th of the solid active $FeCl_2$ on the anode. Therefore, we believe that instead of reduction and oxidation of Fe^{2+} ions in the electrolyte, the Fe/$FeCl_2$ electrode experiences a reversible solid-to-solid transition during each charge-discharge cycle. In such a process, all the Fe or $FeCl_2$ particles form locally and do not grow as dendrites during cycling.

In Fig. 5 (a) and (b) the morphological evolution of Fe and $FeCl_2$ particles in this solid-solid transition process was captured by SEM images. $FeCl_2$ particles, prior to being incorporated in a cell, are all rod-like particles with a diameter of about 1 μm (see Fig. 5 (a) and its inset). After the first charge, these particles turn into moderately flocculated Fe particles of approximately the same size (see Fig. 5 (b) and its inset).

3.4. Cost effectiveness for large-scale energy storage

The cost effectiveness of the Fe/Graphite battery described in this study will make it highly attractive in the commercial energy storage market. Graphite and iron are cheaply available whereas the $NaAlCl_4$ electrolyte can be easily synthesized by reacting equimolar quantities of NaCl and $AlCl_3$ [43]. In Table S1, the individual and cumulative cost of different materials (including Fe current collector, $FeCl_2$, graphite and the electrolyte) in the Fe/Graphite battery is listed. From this it was determined that the total materials CAPEX of this battery will be 33.9 $ kWh^{-1}, and the energy density of the Fe/Graphite battery is estimated to be about ~40 Wh kg^{-1}, which is comparable to the lead–acid battery (based on the cathode capacity of 100 mAh g^{-1}).

However, the cost of the GF is much higher than that of bulk graphite or graphite powder (GP). In order to reduce the cost of the Fe/Graphite battery, a new $FeCl_2$-excess cell was assembled with a FF anode and a GP cathode. Fig. S6 (a) shows the cycling performance of this cell for 80 cycles. The cell has an average Coulombic efficiency of 97.3% at the current density of 3000 mA g^{-1} for graphite. Additionally, the reversible specific capacity of GP at the first cycle reached ~100 mAh g^{-1} with the Coulombic efficiency of 99.70%, which can be seen from the voltage curve at the first cycle in Fig. S6 (c). Similar to the above-mentioned voltage curves of typical $FeCl_2$-excess cells, like Fig. 3 (d) and Fig. S3 (a), the high Coulombic efficiency of 99.70% verifies that the maximum specific capacity of GP cathode is not less than 100 mAh g^{-1} at the current density of 3000 mA g^{-1}.

Then a graphite-excess FP-GP cell was assembled and tested by cyclically charging and diacharging at current density of 3000 mA g^{-1} for graphite (or at 37.5C). As shown in Fig. S6 (b), the cell has been cycled for more than 330 cycles with a capacity retention rate of 82.4%. Also Fig. S6 (d) presents the voltage curves at different cycles during cycling.

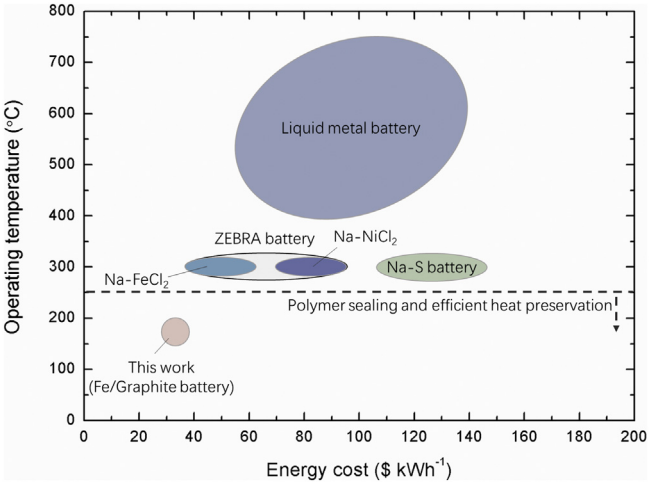

Fig. 6. The material cost and operating temperature comparison of Fe/Graphite cell, ZEBRA battery, Na–S battery, and liquid metal battery [10,11,52–55]. The material cost of Na–S battery is calculated as the one-fourth of a total Na–S battery system.

Although the capacity retention performance of the cell with a GP cathode was not as good as that of the cell with a GF cathode, the maximum specific capacity of GP is almost the same as GF. And we believe that the capacity retention performance of the cell with the low cost GP cathode will be significantly enhanced by optimizing the size, crystallinity, and defect density of graphite particles [36,37,44–51].

Besides, as shown as Fig. S2 (c), the energy efficiency of Fe/Graphite cell is about 70% ~ 80% as the rate of cycling changing from 40C to 120C, which shows an energy storage efficiency between liquid metal batteries and ZEBRA batteries (or Na–S battery). However, the cost of Fe/Graphite batteries is undoubtedly lower than the liquid metal batteries, ZEBRA batteries and Na–S batteries, since only earth-abundant and cheap elements are used (lower CAPEX), with low operating temperatures (lower OPEX) and comparable cycling ability.

As shown in Fig. 6, the materials cost and operating temperature of the Fe/Graphite cell compare favorably with other molten salt batteries. In the future, if the performance and quality of the cathode can be optimized, the life cycle cost of the cell can be further minimized.

4. Conclusion

In summary, we have developed an intermediate-temperature Fe/Graphite battery using an Fe/$FeCl_2$ anode, chloro-basic $NaAlCl_4$/NaCl molten salt electrolyte and graphite foam cathode, operating at 170 °C, which has a capacity retention rate of 85% after nearly 10,000 cycles, with rate capability up to 120C. It was determined that the absence of dendritic growth on Fe metal anode can be attributed to the high reversibility of Fe⇔$FeCl_2$ solid state transformation. Also, it was demonstrated that a slightly graphite-excess electrode capacity matching strategy is ideal for protecting the cell from dangers associated with overcharging. Finally, the battery has a relatively low energy storage cost of 33.9 $ kWh^{-1} as it employs cheap components. With these attributes the Fe/Graphite cell promises to be an effective solution for grid-scale energy storage.

Acknowledgements

This work was supported by the grants from National Natural Science Foundation of China (51874228, U1766216). JL acknowledges support by Wuxi Weifu Inc. Authors acknowledge the International Joint Laboratory for Micro/Nano Manufacturing and Measurement Technologies for the testing service.

Appendix A. Supplementary data

Supplementary data to this article can be found online at https://doi.org/10.1016/j.ensm.2019.09.008.

Conflicts of interest

Authors declare no competing interests.

References

[1] H. Chen, T.N. Cong, W. Yang, C. Tan, Y. Li, Y. Ding, Progress in electrical energy storage system: a critical review, Prog. Nat. Sci. 19 (2009) 291–312. https://doi.org/10.1016/j.pnsc.2008.07.014.
[2] Z. Yang, J. Zhang, M.C. Kintner-Meyer, X. Lu, D. Choi, J.P. Lemmon, J. Liu, Electrochemical energy storage for green grid, Chem. Rev. 111 (2011) 3577–3613. https://doi.org/10.1021/cr100290v.
[3] C.J. Barnhart, S.M. Benson, On the importance of reducing the energetic and material demands of electrical energy storage, Energy Environ. Sci. 6 (2013) 1083–1092. https://doi.org/10.1039/c3ee24040a.
[4] B. Dunn, H. Kamath, J.-M. Tarascon, Electrical energy storage for the grid: a battery of choices, Science 334 (2011) 928–935. https://doi.org/10.1126/science.1212741.
[5] G.L. Soloveichik, Battery technologies for large-scale stationary energy storage, Annu. Rev. Chem. Biomol. Eng. 2 (2011) 503–527. https://doi.org/10.1146/annurev-chembioeng-061010-114116.
[6] J.T. Kummer, N. Weber, A sodium-sulfur secondary battery, SAE Trans. 76 (1968) 1003–1028. https://doi.org/10.4271/670179.
[7] T. Nakabayashi, Sodium sulfur storage battery, 1973, U.S. Patent 3,837,918.
[8] R.J. Bones, J. Coetzer, R.C. Galloway, D.A. Teagle, A sodium/iron (II) chloride cell with a beta alumina electrolyte, J. Electrochem. Soc. 134 (1987) 2379–2382. https://doi.org/10.1149/1.2100207.
[9] B. V Ratnakumar, A.I. Attia, G. Halpert, Sodium metal chloride battery research at the Jet Propulsion Laboratory (JPL), J. Power Sources 36 (1991) 385–394. https://doi.org/10.1016/0378-7753(91)87014-3.
[10] H. Kim, D.A. Boysen, J.M. Newhouse, B.L. Spatocco, B. Chung, P.J. Burke, D.J. Bradwell, K. Jiang, A.A. Tomaszowska, K. Wang, W. Wei, L.A. Ortiz, S.A. Barriga, S.M. Poizeau, D.R. Sadoway, Liquid metal batteries: past, present, and future, Chem. Rev. 113 (2013) 2075–2099. https://doi.org/10.1021/cr300205k.
[11] K. Wang, K. Jiang, B. Chung, T. Ouchi, P.J. Burke, D.A. Boysen, D.J. Bradwell, H. Kim, U. Muecke, D.R. Sadoway, Lithium-antimony-lead liquid metal battery for grid-level energy storage, Nature 514 (2014) 348–350. https://doi.org/10.1038/nature13700.
[12] G. Li, X. Lu, J.Y. Kim, K.D. Meinhardt, H.J. Chang, N.L. Canfield, V.L. Sprenkle, Advanced intermediate temperature sodium-nickel chloride batteries with ultra-high energy density, Nat. Commun. 7 (2016) 10683. https://doi.org/10.1038/ncomms10683.
[13] H.J. Chang, X. Lu, J.F. Bonnett, N.L. Canfield, S. Son, Y.-C. Park, K. Jung, V.L. Sprenkle, G. Li, Development of intermediate temperature sodium nickel chloride rechargeable batteries using conventional polymer sealing technologies, J. Power Sources 348 (2017) 150–157. https://doi.org/10.1016/j.jpowsour.2017.02.059.
[14] K.C. Divya, J. Østergaard, Battery energy storage technology for power systems—an overview, Electr. Power Syst. Res. 79 (2009) 511–520. https://doi.org/10.1016/j.epsr.2008.09.017.
[15] F. Lantelme, H. Groult, Molten Salts Chemistry: from Lab to Applications, Newnes, Burlington, 2013.
[16] X. Lu, B.W. Kirby, W. Xu, G. Li, J.Y. Kim, J.P. Lemmon, V.L. Sprenkle, Z. Yang, Advanced intermediate-temperature Na–S battery, Energy Environ. Sci. 6 (2013) 299–306. https://doi.org/10.1039/c2ee23606k.
[17] Y. Jin, K. Liu, J. Lang, D. Zhuo, Z. Huang, C. Wang, H. Wu, Y. Cui, An intermediate temperature garnet-type solid electrolyte-based molten lithium battery for grid energy storage, Nat. Energy 3 (2018) 732–738. https://doi.org/10.1038/s41560-018-0198-9.
[18] R. Huggins, Advanced Batteries: Materials Science Aspects, Springer Science & Business Media, New York, 2008.
[19] Q. Li, N.J. Bjerrum, Aluminum as anode for energy storage and conversion: a review, J. Power Sources 110 (2002) 1–10. https://doi.org/10.1016/S0378-7753(01)01014-X.
[20] Z. Li, J. Huang, B. Yann Liaw, V. Metzler, J. Zhang, A review of lithium deposition in lithium-ion and lithium metal secondary batteries, J. Power Sources 254 (2014) 168–182. https://doi.org/10.1016/j.jpowsour.2013.12.099.
[21] C.L. Bender, B. Jache, P. Adelhelm, J. Janek, Sodiated carbon: a reversible anode for sodium–oxygen batteries and route for the chemical synthesis of sodium superoxide (NaO_2), J. Mater. Chem. 3 (2015) 20633–20641. https://doi.org/10.1039/c5ta06640a.
[22] A. Manthiram, X. Yu, Ambient temperature sodium-sulfur batteries, Small 11 (2015) 2108–2114. https://doi.org/10.1002/smll.201403257.
[23] P. Bai, J. Li, F.R. Brushett, M.Z. Bazant, Transition of lithium growth mechanisms in liquid electrolytes, Energy Environ. Sci. 9 (2016) 3221–3229. https://doi.org/10.1039/c6ee01674j.
[24] X.B. Cheng, R. Zhang, C.Z. Zhao, Q. Zhang, Toward safe lithium metal anode in rechargeable batteries: a review, Chem. Rev. 117 (2017) 10403–10473. https://doi.org/10.1021/acs.chemrev.7b00115.
[25] S. Li, M. Jiang, Y. Xie, H. Xu, J. Jia, J. Li, Developing high-performance lithium metal anode in liquid electrolytes: challenges and progress, Adv. Mater. 30 (2018) 1706375. https://doi.org/10.1002/adma.201706375.
[26] J.S. Weaving, S.W. Orchard, Experimental studies of transition metal chloride electrodes in undivided cells using molten $NaAlCl_4$ electrolyte, J. Power Sources 36 (1991) 537–546. https://doi.org/10.1016/0378-7753(91)80079-D.
[27] P.J. Tumidajski, M. Blander, Solubility of $FeCl_2$ in molten NaCl–$AlCl_3$, Can. Metall. Q. 31 (1992) 25–30. https://doi.org/10.1179/cmq.1992.31.1.25.
[28] J. Coetzer, G.D. Wald, S.W. Orchard, Mechanism of the cathode reaction in sodium-ferrous chloride secondary cells, J. Appl. Electrochem. 23 (1993) 790–800. https://dx.doi.org/10.1007/BF00249951.
[29] M.C. Lin, M. Gong, B. Lu, Y. Wu, D.Y. Wang, M. Guan, M. Angell, C. Chen, J. Yang, B.J. Hwang, H. Dai, An ultrafast rechargeable aluminium-ion battery, Nature 520 (2015) 324–328. https://dx.doi.org/10.1038/nature14340.
[30] H. Sun, W. Wang, Z. Yu, Y. Yuan, S. Wang, S. Jiao, A new aluminium-ion battery with high voltage, high safety and low cost, Chem. Commun. 51 (2015) 11892–11895. https://dx.doi.org/10.1039/c5cc00542f.
[31] Y. Wu, M. Gong, M. Lin, C. Yuan, M. Angell, L. Huang, D. Wang, X. Zhang, J. Yang, B. Hwang, 3D graphitic foams derived from chloroaluminate anion intercalation for ultrafast aluminum-ion battery, Adv. Mater. 28 (2016) 9218–9222, c10.1002/adma.201602958.
[32] M.L. Agiorgousis, Y.Y. Sun, S. Zhang, The role of ionic liquid electrolyte in an aluminum–graphite electrochemical cell, ACS Energy Lett. 2 (2017) 689–693. https://dx.doi.org/10.1021/acsenergylett.7b00110.
[33] M. Angell, C.J. Pan, Y. Rong, C. Yuan, M.C. Lin, B.-J. Hwang, H. Dai, High Coulombic efficiency aluminum-ion battery using an AlCl3-urea ionic liquid analog electrolyte, Proc. Natl. Acad. Sci. 144 (2017) 834–839. https://dx.doi.org/10.1073/pnas.1619795114.
[34] Y. Song, S. Jiao, J. Tu, J. Wang, Y. Liu, H. Jiao, X. Mao, Z. Guo, D.J. Fray, A long-life rechargeable Al ion battery based on molten salts, J. Mater. Chem. 5 (2017) 1282–1291. https://dx.doi.org/10.1039/c6ta09829k.
[35] W. Weppner, R.A. Huggins, Ionic conductivity of solid and liquid $LiAlCl_4$, J. Electrochem. Soc. 124 (1977) 35–38. https://dx.doi.org/10.1149/1.2133238.
[36] H. Chen, H. Xu, S. Wang, T. Huang, J. Xi, S. Cai, F. Guo, Z. Xu, W. Gao, C. Gao, Ultrafast all-climate aluminum-graphene battery with quarter-million cycle life, Sci. Adv. 3 (2017) eaao7233. https://dx.doi.org/10.1126/sciadv.aao7233.
[37] L. Zhang, L. Chen, H. Luo, X. Zhou, Z. Liu, Large-sized few-layer graphene enables an ultrafast and long-life aluminum-ion battery, Adv. Energy Mater. 7 (2017) 1700034. https://dx.doi.org/10.1002/aenm.201700034.
[38] L. Qingfeng, Electroless growth of aluminum dendrites in NaCl-$AlCl_3$ melts, J. Electrochem. Soc. 136 (1989) 2940–2943. https://dx.doi.org/10.1149/1.2096377.
[39] L. Qingfeng, Electrochemical deposition of aluminum from NaCl-$AlCl_3$ melts, J. Electrochem. Soc. 137 (1990) 593–598. https://dx.doi.org/10.1149/1.2086512.
[40] P.R. Gifford, J.B. Palmisano, An aluminum/chlorine rechargeable cell employing a room temperature molten salt electrolyte, J. Electrochem. Soc. 135 (1988) 650–654. https://dx.doi.org/10.1149/1.2095685.
[41] K.S. Mohandas, N. Sanil, M. Noel, P. Rodriguez, Anodic behaviour of carbon materials in NaCl saturated $NaAlCl_4$ fused electrolyte at low temperatures: a cyclic voltammetric study, J. Appl. Electrochem. 31 (2001) 997–1007. https://dx.doi.org/10.1023/A:1017966316057.

[42] T. Javadi-Doodran, Microstructure and Conductivity of the Sodium Nickel Chloride (ZEBRA) Battery Cathode, Doctoral dissertation, McMaster University, 2012. September.
[43] N.C. Baenziger, The crystal structure of $NaAlCl_4$, Acta Crystallogr. 4 (1951) 216–219. https://dx.doi.org/10.1107/S0365110X5100074X.
[44] C. Hao, G. Fan, Y. Liu, T. Huang, B. Zheng, N. Ananth, X. Zhen, W. Gao, G. Chao, A defect-free principle for advanced graphene cathode of aluminum-ion battery, Adv. Mater. 29 (2017) 1605958. https://dx.doi.org/10.1002/adma.201605958.
[45] D.Y. Wang, C.Y. Wei, M.C. Lin, C.J. Pan, H.L. Chou, H.A. Chen, M. Gong, Y. Wu, C. Yuan, M. Angell, Y.J. Hsieh, Y.H. Chen, C.Y. Wen, C.W. Chen, B.J. Hwang, C.C. Chen, H. Dai, Advanced rechargeable aluminium ion battery with a high-quality natural graphite cathode, Nat. Commun. 8 (2017) 14283. https://dx.doi.org/10.1038/ncomms14283.
[46] X. Yu, B. Wang, D. Gong, Z. Xu, B. Lu, Graphene nanoribbons on highly porous 3D graphene for high-capacity and ultrastable Al-ion batteries, Adv. Mater. 29 (2017) 1604118. https://dx.doi.org/10.1002/adma.201604118.
[47] C. Jiang, Y. Fang, W. Zhang, X. Song, J. Lang, L. Shi, Y. Tang, A multi-ion strategy towards rechargeable sodium-ion full batteries with high working voltage and rate capability, Angew. Chem. 57 (2018) 16370. https://dx.doi.org/10.1002/anie.201810575.
[48] M. Wang, C. Jiang, S. Zhang, X. Song, Y. Tang, H. Cheng, Reversible calcium alloying enables a practical room-temperature rechargeable calcium-ion battery with a high discharge voltage, Nat. Chem. 10 (2018) 667–672. https://dx.doi.org/10.1038/s41557-018-0045-4.
[49] Q. Liu, H. Wang, C. Jiang, Y. Tang, Multi-ion strategies towards emerging rechargeable batteries with high performance, Energy Storage Mater. (2019). https://dx.doi.org/10.1016/j.ensm.2019.03.028.
[50] G. Zhang, X. Ou, C. Cui, J. Ma, J. Yang, Y. Tang, High-performance cathode based on self-templated 3D porous microcrystalline carbon with improved anion adsorption and intercalation, Adv. Funct. Mater. 29 (2019) 1806722. https://dx.doi.org/10.1002/adfm.201806722.
[51] M. Zhang, X. Song, X. Ou, Y. Tang, Rechargeable batteries based on anion intercalation graphite cathodes, Energy Storage Mater. 16 (2019) 65–84. https://dx.doi.org/10.1016/j.ensm.2018.04.023.
[52] The Electric Power Research Institute, Energy Storage Cost Summary for Utility Planning: Executive Summary, 2016. https://www.epri.com/#/pages/product/3002008877/ (accessed March 2019).
[53] G. Li, X. Lu, J.Y. Kim, V. V Viswanathan, K.D. Meinhardt, M.H. Engelhard, V.L. Sprenkle, An advanced Na-$FeCl_2$ ZEBRA battery for stationary energy storage application, Adv. Energy Mater. 5 (2015) 1500357. https://dx.doi.org/10.1002/aenm.201500357.
[54] X. Ning, S. Phadke, B. Chung, H. Yin, P. Burke, D.R. Sadoway, Self-healing Li–Bi liquid metal battery for grid-scale energy storage, J. Power Sources 275 (2015) 370–376. https://dx.doi.org/10.1016/j.jpowsour.2014.10.173.
[55] T. Ouchi, H. Kim, B.L. Spatocco, D.R. Sadoway, Calcium-based multi-element chemistry for grid-scale electrochemical energy storage, Nat. Commun. 7 (2016) 10999. https://dx.doi.org/10.1038/ncomms10999.